Journal of Materials Research and Technology 40 (2026) 1518–1527

Contents lists available at ScienceDirect

Journal of Materials Research and Technology

journal homepage: www.elsevier.com/locate/jmrt

Back stress evolution as a function of prestrain in a nickel-based superalloy

Mohit M. Ludhwani [a,b,*], Fumiyoshi Yoshinaka [b], Tsubasa Tokuzumi [b], Rintaro Ueji [b,**], Anand K. Kanjarla [a,***]

[a] Department of Metallurgical and Materials Engineering, IIT Madras, Chennai, India
[b] NIMS, Tsukuba, Japan

ARTICLE INFO

Keywords:
Back stress
Bauschinger effect
IN718
Geometrically necessary dislocation (GND)
Kernel misorientation (KAM) angle
Σ3 boundaries

ABSTRACT

Back stress, an internal stress linked to dislocation interactions with microstructural features, plays a crucial role in governing the Bauschinger effect in metals. Although the deformation behaviour of IN718 has been widely investigated, the influence of prestrain applied on back stress evolution in aged IN718 remains insufficiently explored. In this study, two complementary approaches are employed: a macroscopic method, defining back stress as half the stress difference between prestrain and reversed yield, and a microscopic method, estimating back stress through geometrically necessary dislocation (GND) density derived from electron backscatter diffraction (EBSD). Both approaches yield consistent results, demonstrating that back stress increases with prestrain, although the rate of evolution differs between low and high prestrain regimes. The change in the rate is likely associated with the evolution of microstructural features during deformation. EBSD analysis reveals substantial microstructural modifications, including an increase in GND density, elevated KAM values, and a gradual loss or transition in character of Σ3 boundaries. Since Σ3 boundaries usually act as efficient dislocation transmitters and accommodate strain, their degradation increases resistance to dislocation transmission, thereby amplifying the evolution of back stress. Incorporating these microstructural observations into a dislocation-based flow stress model enables a direct linkage between the macroscopic mechanical response and the underlying microstructural variations. These findings highlight the critical role of Σ3 boundaries in controlling the development of back stress, providing insights into the interplay among prestrain, microstructure, and mechanical behaviour in aged IN718.

1. Introduction

Inconel 718 (IN718) is a γ" precipitate-strengthened nickel-based superalloy with excellent mechanical properties, corrosion and oxidation resistance at elevated temperatures. The microstructure of IN718 usually consists of disk-shaped γ" (Ni_3Nb) precipitates (20–30 nm in diameter and 5–6 nm thickness) and spherical γ' ($Ni_3(Al/Ti)$) precipitates distributed in γ matrix [1]. IN718 is used to manufacture rotating aerospace components, such as shafts, turbine blades, and compressor discs [1]. These components experience cyclic loading during their application. During load reversal, the yield stress is typically lower than in forward loading, a phenomenon known as the Bauschinger effect [2]. This effect is attributed to the generation of back stress due to heterogeneous plastic deformation and the subsequent evolution of dislocation substructures.

Several studies have investigated back stress in polycrystalline materials, including copper [3,4], nickel [5], aluminium [6], and steel [4,6]. In single-phase materials, dislocation interactions with grain boundaries generate back stress. In dispersed or precipitate-strengthened alloys, interactions with precipitates also influence the generation of back stress. It is well known that these interactions can be classified as Orowan looping or shearing. Orowan looping [7], which occurs with large incoherent precipitates, significantly increases back stress, while small coherent precipitates undergoing shearing are assumed not to affect back stress. However, recent research has shown that small coherent precipitates can generate back stress due to a local gradient in precipitate density [8]. This highlights the role of precipitates in generating back stress, which can vary depending on material composition and deformation conditions.

Prior research on nickel-based superalloys has examined how factors

* Corresponding author. Department of Metallurgical and Materials Engineering, IIT Madras, Chennai, India.
** Corresponding author.
*** Corresponding author.
E-mail addresses: mm20d008@smail.iitm.ac.in (M.M. Ludhwani), ueji.rintaro@nims.go.jp (R. Ueji), kanjarla@iitm.ac.in (A.K. Kanjarla).

https://doi.org/10.1016/j.jmrt.2025.12.237
Received 3 November 2025; Received in revised form 8 December 2025; Accepted 22 December 2025
Available online 23 December 2025

such as strain rate and precipitation influence the Bauschinger effect. For example, a study on the nickel-based superalloy Haynes 230 [9] demonstrated that the Bauschinger effect appears only at high strain rates in the solution-annealed condition. In contrast, it persists across all strain rates in the precipitate-strengthened condition. This difference was attributed to the higher dislocation density generated by precipitates, leading to stronger back stress. Another study by Valle et al. [10] has reported the Bauschinger effect in another γ' strengthened nickel-based superalloy, Inconel X-750, in solution-annealed, aged and overaged conditions. They observed that the Bauschinger effect increased with increasing aging time, and for different precipitate sizes, the back stress value increased with increasing prestrain. Similarly, the back stress evolution is explored in solution-annealed IN718 when subjected to the cyclic loading-unloading test [11]. An increase in back stress was observed with an increase in prestrain for almost all mean grain sizes. Kreins et al. [12] investigated the effect of γ" volume fraction on the Bauschinger effect in IN718, discovering that increased volume fraction of γ" reduced the Bauschinger effect, likely due to additional slip systems being activated and decreased incompatibility at grain boundaries. However, the Bauschinger effect was studied at one prestrain value of 2 %, followed by compression. While this study provides valuable insights, it primarily focuses on specific prestrain conditions, leaving the effect of varying prestrain on back stress in aged IN718 unexplored. Increasing prestrain generally leads to more significant dislocation generation, contributing to higher back stress [13,14]. He et al. observed that the total dislocation density increases with increasing prestrain in solution-annealed IN718 [11]. Kreins et al. studied variations in geometrically necessary dislocations (GND) density variation in γ" precipitate for polycrystal-aged IN718 [12]. Back stress can be related to the generation of GND [15]. However, the direct relation of GND density to back stress in IN718 polycrystals has yet to be explored.

The present study addresses these gaps by systematically investigating the effect of varying prestrain on the evolution of back stress in aged IN718. This aspect has been previously unexplored in the literature. Back stress evolution is examined using tension (prestrain)–compression tests at different prestrain levels, combined with detailed microstructural characterization via EBSD. Furthermore, this work compares two distinct approaches for quantifying back stress: one based on the macroscopic stress–strain response and the other derived from measurements of GND density. By establishing a direct correlation between GND density and back stress, and by evaluating the concurrent evolution of Σ3 boundaries, this study provides new insights into the microstructural mechanisms governing the development of back stress in aged IN718. Additionally, the possible mechanisms underlying the variation in back stress at both small and high prestrains are discussed.

2. Experiments

The nickel-based superalloy, IN718, was received in a forged condition. The chemical composition of IN718 and the heat treatment process are summarised in Table 1. The heat treatment process with two stages was conducted to prepare the specimen for the mechanical tests: (1) solution annealing at a temperature of 1050 °C for 1 h, aimed at dissolving the alloying elements, followed by water quenching, and (2) double aging to facilitate precipitation. The double aging procedure involves a holding period at 720 °C for 8 h, followed by furnace cooling to 620 °C at a rate of 55 °C per hour over 2 h. This is then accompanied by an additional 8-h holding period at 620 °C, concluding with air cooling [12]. The heat-treated samples were subjected to different tensile prestrain: 0.5 %, 1.5 %, 7 %, and 10 %. The selection of small prestrain values is intended for understanding back stress at the onset of plastic deformation, while high prestrain values are used to understand back stress at an advanced stage of plastic deformation. Lower prestrains capture the initial build-up of internal stresses, while higher prestrains reflect the influence of accumulated dislocation structures and microstructural evolution on back stress.

Table 1
Chemical composition of IN718 and heat treatment.

Elements	Ni	Fe	Cr	Nb	Al	Ti	C
Wt %	53.37	18.62	18.19	4.89	0.50	1.04	0.02
Heat treatment	Solution annealing (1050 °C (1h)) + Water quenching + Double aging (720 °C (8h) cool to 620 °C with 55 °C/h cooling rate (2h) + 620 °C (8h) + Air cooling						

A cylindrical dog-bone specimen was used for prestrain. Following prestrain, cylindrical compression specimens were extracted from the gauge region while maintaining a length-to-diameter (L/D) ratio of 1.5. Both tensile and compression tests were performed at a strain rate of $1 \times 10^{-3}\ s^{-1}$ at room temperature. Although IN718 is primarily utilised for high-temperature applications, the present study focuses on room-temperature deformation to isolate the intrinsic dislocation–microstructure interactions governing back stress evolution. Establishing this baseline understanding at room temperature provides a fundamental framework for interpreting the alloy's mechanical response under more complex high-temperature conditions. Microstructural characterisation of the prestrained samples was conducted using scanning electron microscopy (SEM) with electron backscatter diffraction (EBSD), utilising a JEOL JSM-7000F system with an accelerating voltage of 15 kV. For EBSD characterisation, the samples underwent mechanical polishing with progressively finer grit papers (400, 800, and 1200) before being electropolished using an electrolyte solution consisting of 10 % acetic acid and 90 % perchloric acid, applied for 20 s at 25 V at room temperature. The inverse pole figure (IPF) map and grain size distribution of the initial microstructure after heat treatment (undeformed condition) are presented in Fig. 1(a) and (b), respectively. The IPF map clarified the presence of two or three annealing twin boundaries per grain.

The EBSD data were further used to analyse kernel average misorientation (KAM) angle maps and GND density. The quantification of GND density from EBSD is influenced by various scanning parameters, including step size, binning, and the area under consideration. The current study utilised a step size of 200 nm and a binning of 8 × 8, which is suitable for determining the GND density. The analysis area designated for GND density calculation measured 350 × 120 μm^2. Additionally, a coarse-step-size EBSD scan was performed over a larger area to assess the grain size distribution and the fraction of different grain boundaries. The MTEX [16,17] toolbox in MATLAB software was used for EBSD data analysis.

3. Evaluation of back stress

The back stress was examined using two methods in this work: (i) The back stress calculated from true stress-strain data obtained by tension (prestrain)-compression test will be called macroscopic back stress (σ_b). (ii) The back stress calculated by gathering the microstructural information (GND) from the EBSD data of prestrained samples will be referred to as the microscopic back stress (σ_{mb}).

3.1. Macroscopic back stress

Following the widely accepted method of back stress estimation [12,18,19], the true stress-strain data evaluated by tension (prestrain) and compression are used to obtain the macroscopic back stress (σ_b) according to the formula in Equation (1).

$$\sigma_b = \left(\sigma_f - \sigma_r\right) / 2 \tag{1}$$

, where σ_f is the maximum stress reached during the prestrain, i.e. the forward straining, and σ_r is the yield stress for the prestrained sample subjected to compression, i.e. the reversed straining. The Bauschinger

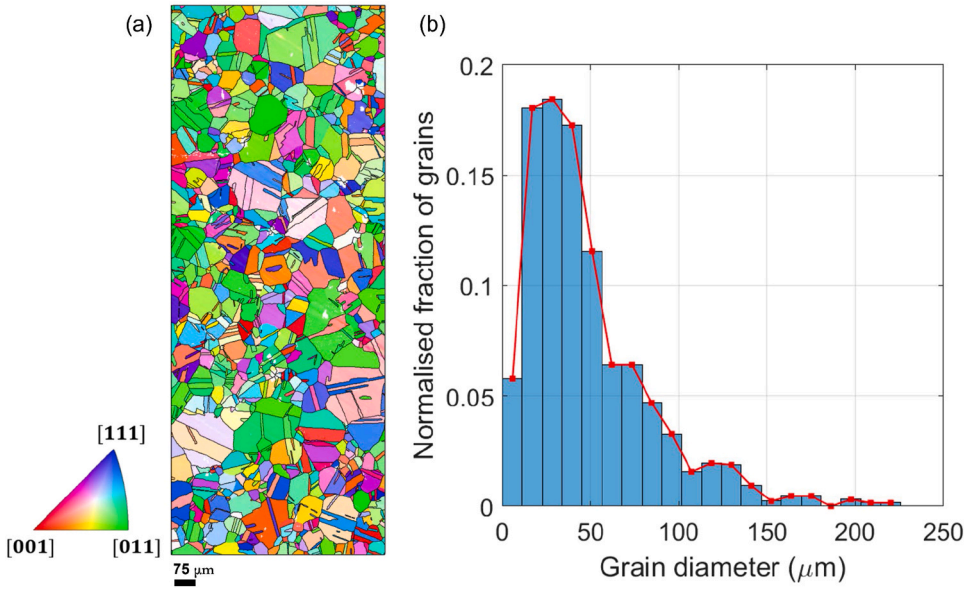

Fig. 1. (a) Inverse pole figure (IPF) map (colour represents crystallographic orientation normal to scanning plane), the black lines represent grain boundaries, and (b) grain size distribution of the material after heat treatment, i.e. undeformed condition obtained from EBSD measurement.

stress parameter (*BSP*) is also obtained to understand the Bauschinger effect by normalising the back stress by the maximum true stress.

$$BSP = (\sigma_f - \sigma_r) \,/\, 2\sigma_f \tag{2}$$

This is a simple phenomenological definition of macroscopic back stress based on the Bauschinger effect. While this approach does not capture the full complexity of microstructure as seen in this alloy, it provides a practical measure for evaluating back stress evolution in aged IN718. To understand the change in backstress at the microscopic level, we employed a microscopic backstress, which is a function of GND density, as discussed in the following section.

3.2. Microscopic back stress

The GND density (ρ_{GND}) is incorporated into Taylor's type equation to evaluate the microscopic back stress (σ_{mb}). A similar approach has been employed to estimate back stress [20,21] using Equation (3).

$$\sigma_{mb} = \sigma_0 + KGb\sqrt{\rho_{GND}} \tag{3}$$

where σ_0 the initial back stress evolved before the examination, K is a scaling constant [22], G represents shear modulus, and b denotes the Burgers vector. It is worth noting that various approaches are presented in the literature for calculating the GND density, as listed in Table 2. The KAM-based and Nye tensor approaches utilise EBSD data to calculate the GND density, whereas Ashby's model relates GND density to plastic shear strain using the empirical formulation. The procedure in MTEX was employed to derive the reduced component of the dislocation density tensor, referred to as the Nye tensor [23,24].

The parameters necessary for calculating GND density for IN718 are outlined in Table 3. σ_0 (~45 MPa) in equation (3) is taken as half the difference between the yield point during tension and the yield point during compression without any prestrain. The current study obtained GND density using all three approaches and subsequently compared them. The results from the tension (prestrain)-compression tests and microstructure analysis are presented in the following sections.

Table 2
The formulas for the different approaches used for GND density calculation.

Approach	Formula	
KAM based [8, 25,26]	$\rho_{GND} = (2\theta)/(bd)$	θ is the misorientation angle, b is the Burgers vector, d is the scan step size
Ashby's model [27,28]	$\rho_{GND} = (4\gamma)/(\lambda_G b)$	γ the plastic shear strain, b is the Burgers vector, λ_G is the average slip distance of dislocationsi. e. grain size in the case of recrystallised fully annealed polycrystalline material
Nye tensor [12, 29,30]	$\rho_{GND} = (1/b)\sqrt{\alpha_{ij}\alpha_{ij}}$	α_{ij} is the dislocation density tensor, b is the Burgers vector,

4. Results

4.1. Macroscopic back stress

The stress-strain curves obtained by the tensile tests subjected to various prestrain are illustrated in Fig. 2(a). The yield point and hardening behaviours remained consistent for all prestrain, indicating good reproducibility in the results. On the other hand, the compression on prestrained samples in Fig. 2(b) exhibits notable variations in yield points.

The maximum stress following tensile prestrain and the yield stress observed during subsequent compression are illustrated as a function of the prestrain in Fig. 3(a). The dotted lines indicate the yield points at tension and compression without prestrain. The yield stress for the compression following prestrain is lower than that during compression without prestrain. The available data is incorporated into equation (2) to derive the macroscopic back stress, and the results are demonstrated in Fig. 3(b). The previous study reported back stress specifically at a prestrain of 2 % [12], and its value aligns well with the observation in the present study. Furthermore, Fig. 3(b) reveals the characteristic behaviour of the evolution of back stress in IN718, which differs from that of commercial high-strength steels [33]. The rate of back stress evolution is lower for prestrain increases from 0.5 % to 1.5 % than from 7 % to 10 %,

Table 3
Parameters used to quantify the average GND.

Parameter	Value
Burgers vector (b) [31,32]	0.256 nm
Shear modulus (G) [31,32]	77200 MPa
The average slip distance (λ_G)	48 μm (mean grain size in initial state)

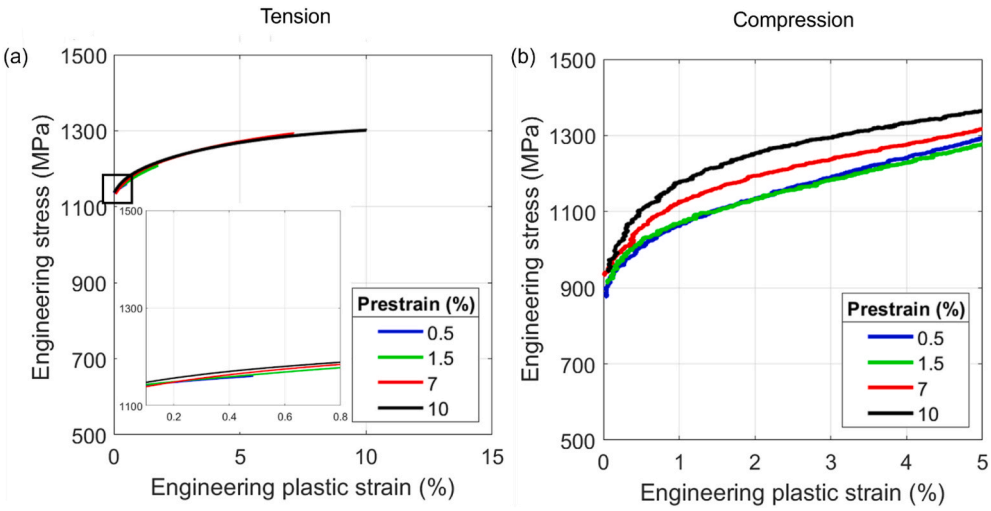

Fig. 2. Stress-strain response obtained by (a) the tensile test for prestrain up to 0.5 %, 1.5 %, 7 %, and 10 %, and (b) the subsequent compression on the pre-strained samples.

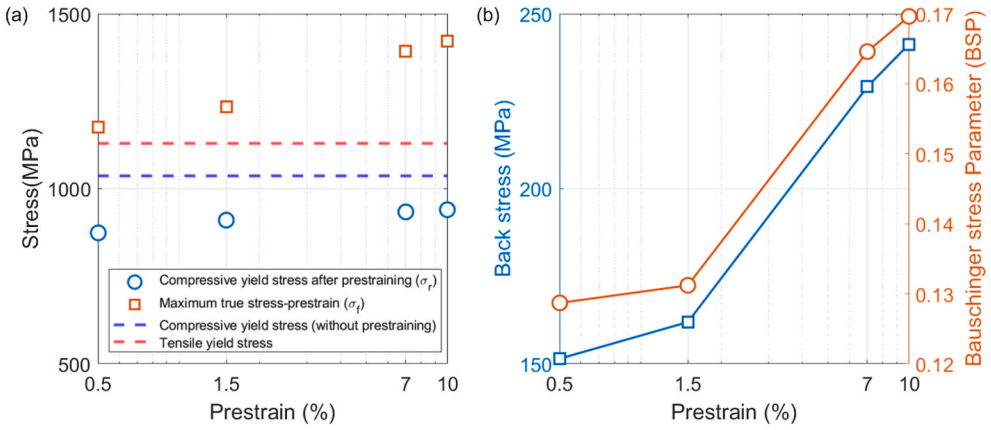

Fig. 3. (a) The maximum stress and yield points after compression with prestrain compared to the original yield points in tension and compression for samples without prestrain. (b) The variation of macroscopic back stress and BSP for prestrain of 0.5 %, 1.5 %, 7 %, and 10 %.

likely due to interactions among microstructural features in IN718. Additionally, the *BSP* is plotted within the same figure, showing a similar trend.

4.2. Microscopic back stress

4.2.1. Microstructure analysis

The results of EBSD measurements are shown in Fig. 4, including (a) orientation and KAM maps, (b) the mean KAM values, and (c) the fraction of Σ3 boundaries. Plastic deformation leads to progressive lattice rotation and the evolution of subgrain structures. The IPF maps in Fig. 4(a) reveal an increasing orientation gradient within grains as prestrain increases. A corresponding rise in the mean KAM value is observed to be significant at prestrain of 7 % and 10 %.

The KAM maps in Fig. 4(a) indicated characteristics of cell block structures commonly observed after plastic deformation in FCC metals [34]. These cell blocks are delineated with geometrically necessary boundaries (GNBs), which appear as extended boundary lines in KAM maps. Such features are pronounced with increasing prestrain, as observed in KAM maps. Additionally, the variation in the fraction of Σ3 boundaries is illustrated in Fig. 4(c). The fraction is reduced with increasing prestrain. This reduction occurs due to the tendency of grain boundaries to evolve as plastic deformation is applied. With increasing prestrain, grain boundaries undergo local grain rotation and dislocation rearrangement. This leads to the transition of Σ3 boundaries into random angle grain boundaries [35,36]. The following section presents the results of the GND density calculation.

4.2.2. GND density

The GND density distribution obtained using the Nye tensor and KAM data for all prestrain followed a one-peak log-normal distribution consistent with previous studies [17,24]. The geometric mean was used to compute the average GND density following the approach of Jiang et al. [24], as it helps prevent potential overestimation associated with the arithmetic mean.

EBSD analysis was performed using a single high-quality scan for each prestrain level, and the resulting GND density and KAM values are reported as representative data for the respective prestrain conditions. To provide a meaningful assessment of the measurement variability, the full distributions of the GND densities are presented together with a box plot summarising their statistical spread in Fig. 5. While this approach does not replace true sample-to-sample statistics, it reflects the internal variability within each scan. As prestrain increases, both methods show a clear upward shift in the median GND density and a broadening of the distribution. The observed evolution—an increase in both the median GND value and the distribution width with increasing prestrain—shows a trend consistent with reports for other FCC alloys, such as Cu and Ni [24,27], which supports the reliability of the EBSD-derived GND data.

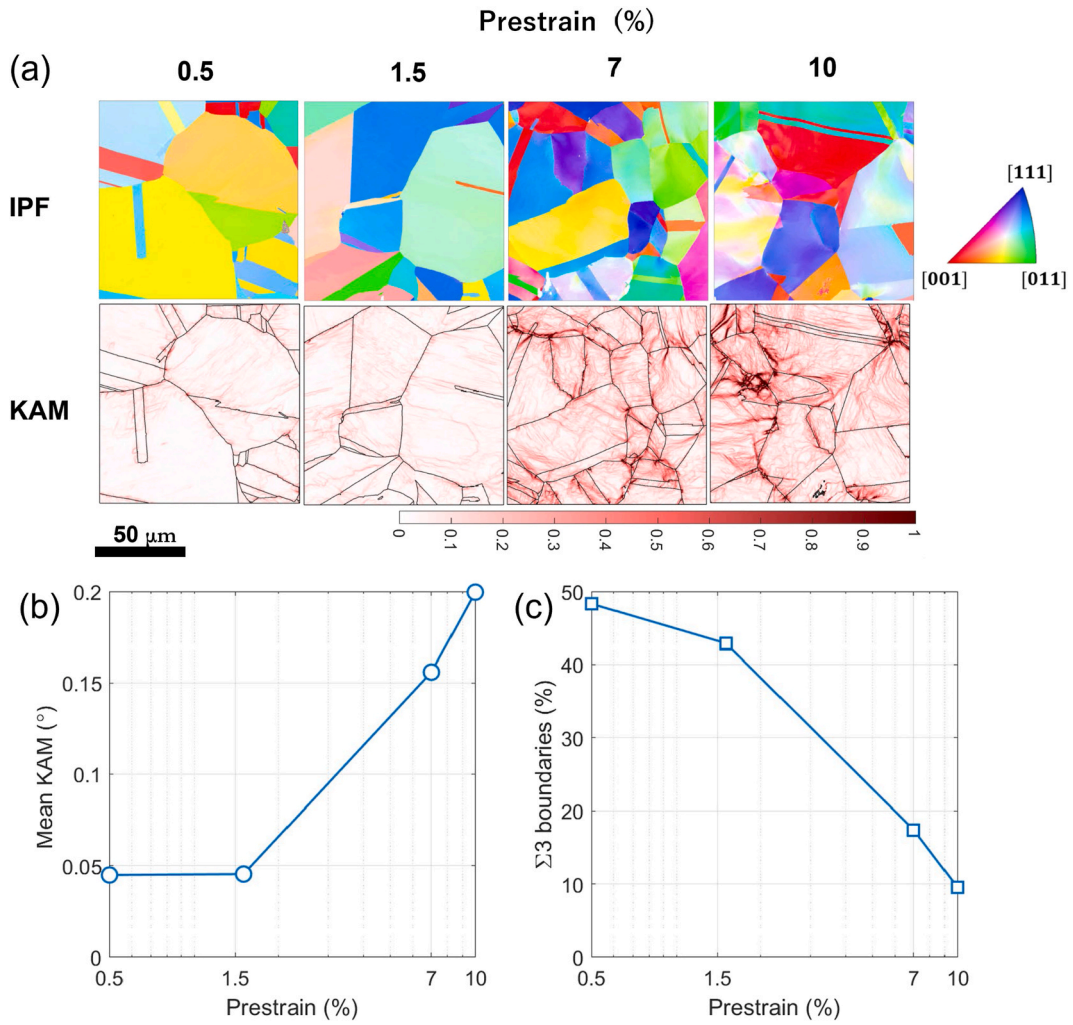

Fig. 4. (a) Inverse pole figure (IPF) maps and corresponding KAM maps (colour represents crystallographic orientation normal to scanning plane), (b) mean KAM values and (c) Σ3 boundary fraction of prestrained samples for prestrain values of 0.5 %,1.5 %,7 % and 10 %.

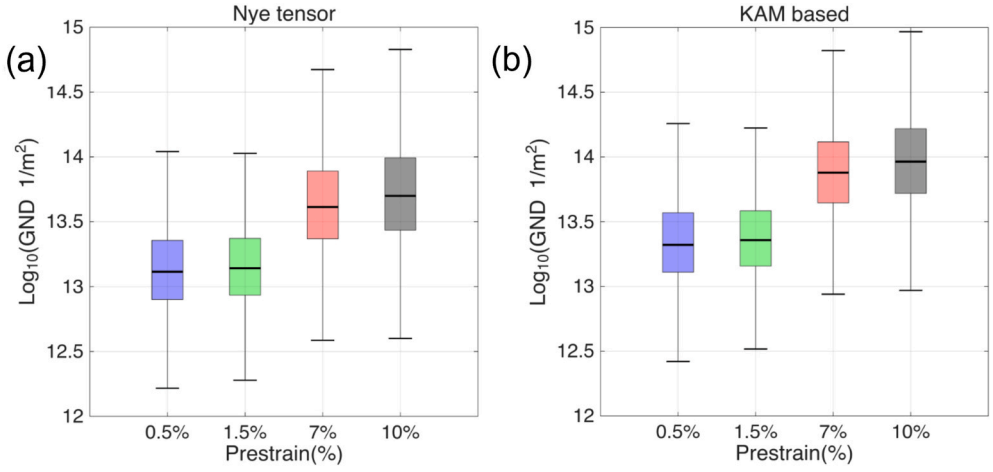

Fig. 5. Box plots of the GND density distributions obtained using the (a) Nye tensor–based method and (b) KAM-based method.

The GND density obtained from the KAM-based calculation, Ashby's model and the Nye tensor is shown in Fig. 6. All approaches exhibit an increase in GND density with increasing prestrain.

4.2.3. Comparison of microscopic back stress and macroscopic back stress

The microscopic back stress is calculated using equation (3). A comparison of microscopic back stress obtained from all approaches and macroscopic back stress is shown in Fig. 7. All approaches demonstrate consistent trends when a uniform scaling constant of K = 0.9 in equation

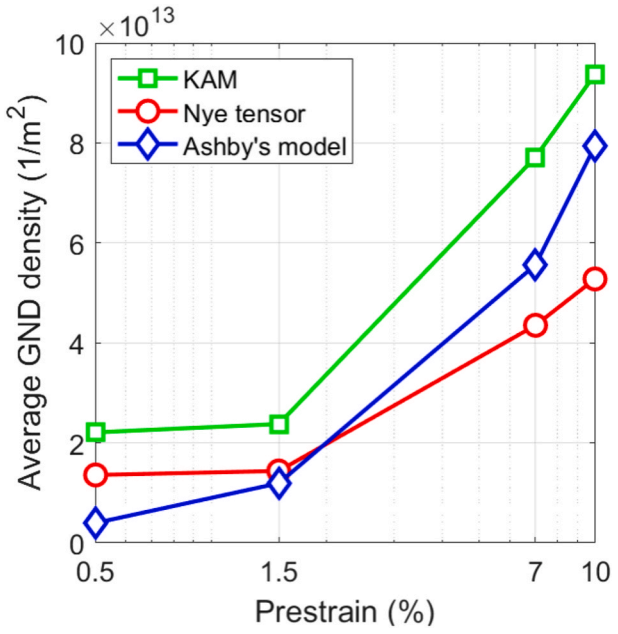

Fig. 6. Average GND density obtained from the KAM-based, Nye tensor and Ashby's model for prestrain values of 0.5 %,1.5 %,7 % and 10 %.

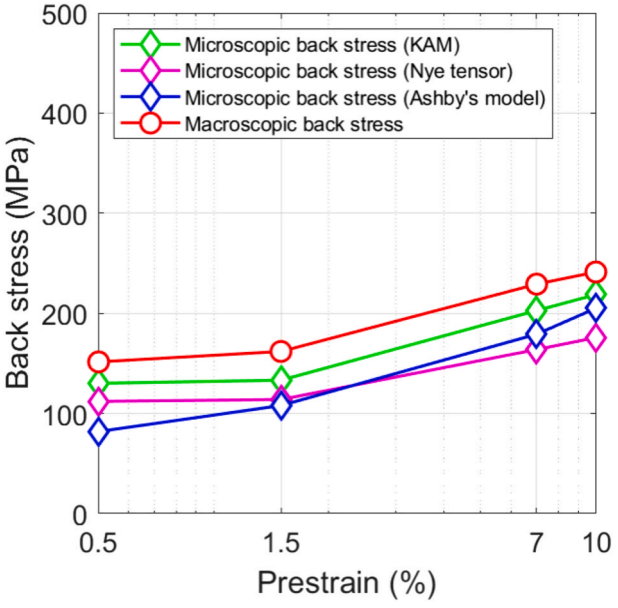

Fig. 7. Comparison of macroscopic back stress with microscopic back stress from the KAM-based, Nye tensor and Ashby's model, and the trend observed in the macroscopic and microscopic back stress is consistent, confirming the reliability of the approaches used.

(3) is applied to align the microscopic back stress with the macroscopic back stress. Here, K acts as a scaling constant used to match the microscopic back stress estimated from the GND density with the macroscopic back stress obtained from mechanical testing. It does not represent a physically independent material parameter but serves as a calibration factor, consistent with earlier dislocation-based modelling approaches [37,38]. The macroscopic and microscopic back stress trends strongly link plastic deformation and dislocation generation. As prestrain increases, macroscopic back stress increases, indicating the evolution of substructure and dislocation. The IPF maps, KAM maps, and GND density calculations exhibit these microstructural evolutions. The reduction in Σ3 boundaries indicates a change in grain boundary structure. These findings might help to explain the mechanisms behind back stress, which are discussed in the next section.

5. Discussion

The experimental results showed that the back stress evolution rate varies with prestrain. Specifically, the back stress increased slowly at lower prestrain (0.5 %–1.5 %) than at higher prestrain (7 %–10 %), as observed in Fig. 3(b). This indicates a transition in the mechanism responsible for generating back stress. This transition is influenced by the microstructural evolution during deformation, including the grain boundary character, dislocation substructures, and γ" precipitate.

A significant number of grain boundaries in IN718 at the initial state are Σ3 boundaries, as many annealing twin boundaries were found in Fig. 1(a). At low prestrain, the Σ3 boundary fraction shows little variation, as shown in Fig. 4(c). The relatively low KAM values near Σ3 boundaries suggest the limited contribution to the back stress via dislocation accumulation at these prestrains. In contrast, at higher prestrain, the fraction of Σ3 boundaries decreases significantly, while the fraction of random grain boundaries increases. This provides additional resistance to dislocation motion and contributes more prominently to back stress. Increased KAM values near random grain boundaries support this trend (Fig. 4(a)).

However, the response of Σ3 boundaries to deformation varies depending on the crystallographic orientation of the adjoining grains. Some Σ3 boundaries remain intact even after deformation, as shown in Fig. 8 (yellow arrow), in the vicinity of which KAM values are low. Such intact Σ3 boundaries appeared limited at the higher prestrain. Conversely, fragmented Σ3 boundaries (red circle) and random boundaries (black arrow) exhibit increased KAM, suggesting intensified dislocation activity. To further elucidate the observed microstructural and mechanical trends, a dislocation-based flow stress model was employed to relate the evolution of flow stress to dislocation density and the fraction of Σ3 boundaries. This model captures the interaction of dislocations with microstructural features, thereby establishing a quantitative framework that links microstructural evolution with macroscopic flow behaviour and enhances the interpretation of back stress development. The governing equations of the model were adapted from Ref. [39], with specific modifications introduced in the mean free path formulation to explicitly account for the influence of Σ3 boundaries on dislocation motion:

$$\sigma_f = \sigma_{fri} + \alpha M G b \sqrt{\rho} \tag{4}$$

$$\frac{d\rho}{d\varepsilon} = M\left(\frac{1}{b\lambda_{eff}} - f\rho\right) \tag{5}$$

$$\Delta\rho = \left(\frac{1}{b\lambda_{eff}} - f\rho\right) M\Delta\varepsilon \tag{6}$$

$$\frac{1}{\lambda_{eff}} = \frac{1}{d} + \frac{1}{l_{\Sigma 3}} + \beta\sqrt{\rho} \tag{7}$$

$$l_{\Sigma 3} = \frac{d}{f_{\Sigma 3}} \tag{8}$$

Where σ_f is the flow stress, σ_{fri} represents the frictional stress contribution from solid-solution and precipitate strengthening, α is geometrical interaction factor, M is taylor factor, ρ is dislocation density, λ_{eff} is the mean free distance, $l_{\Sigma 3}$ is effective Σ3 boundaries length, $f_{\Sigma 3}$ is the fraction of Σ3 boundaries (obtained from EBSD shown in Fig. 4(c)), d is average grain size, f is dynamic recovery parameter and β is an obstacle constant. The material parameters corresponding to the 10 % prestrain condition are listed in Table 4.

In this work, a value of α = 0.9 is used. Reported α values for FCC

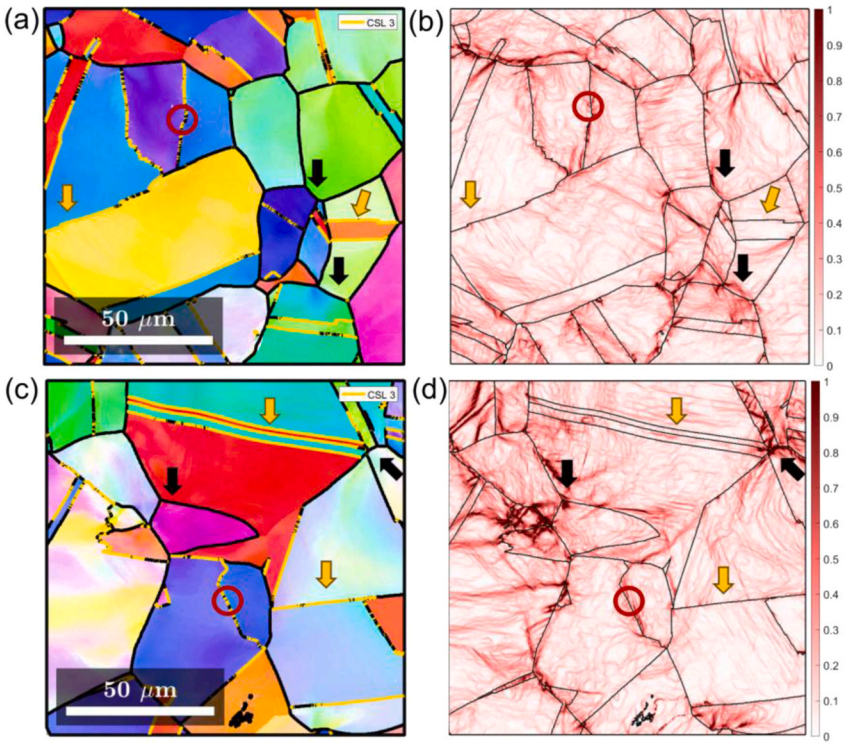

Fig. 8. Inverse pole figure (IPF) maps showing Σ3 grain boundaries (yellow lines) and random grain boundaries (black lines) for prestrain of 7 % and 10 % in (a) and (c), respectively. The corresponding KAM maps in (b) and (d) show lower KAM values at Σ3 boundaries and increased KAM at random grain boundaries.

Table 4
Values of model parameters used for fitting the model with experimental true stress-strain data for 10 % prestrain condition.

Parameter	Value
Initial dislocation density (ρ_0)	1×10^{11} ($1/m^2$) [31]
σ_{fric}	1070 (MPa)
β	0.0035
f	0.8
α	0.9
M	3.06 [39]

metals span a wide range (approximately 0.16–1.1 [40]), as the parameter reflects the strength of dislocation–dislocation interactions. For Ni-based superalloys such as IN718, the literature also shows considerable variation: some studies employ α values close to unity [41], whereas others report much smaller values (α ≈ 0.01) [31]. Because the exact contributions of the various interaction mechanisms cannot be directly quantified in the present study, α is treated as an effective parameter and selected within the established FCC range to ensure consistency between the model predictions and the experimentally measured flow stress. Another parameter considered as input in the modelling is the Σ3 boundary fraction, which was experimentally measured at four prestrain (0.5 %, 1.5 %, 7 % and 10 %). These discrete values were fitted using an exponential decay relation to obtain a continuous Σ3–strain function, as shown in Fig. 9.

This fitted curve allows the estimation of the Σ3 fraction at any intermediate strain. The continuous Σ3 (prestrain) evolution was then used as input to the dislocation-based constitutive model to compute the evolution of dislocation density and the corresponding flow stress response over the full strain range. The material parameters were calibrated using the 10 % prestrain condition, and the corresponding true stress–true strain response is shown in Fig. 10, demonstrating good agreement between the experimental data and the model prediction. Using the same parameter set, the true stress-strain curves for 0.5 %, 1.5 %, and 7 % prestrain levels were predicted. These results are presented in Fig. 11, along with the respective experimental curves, which show good agreement across all prestrain conditions.

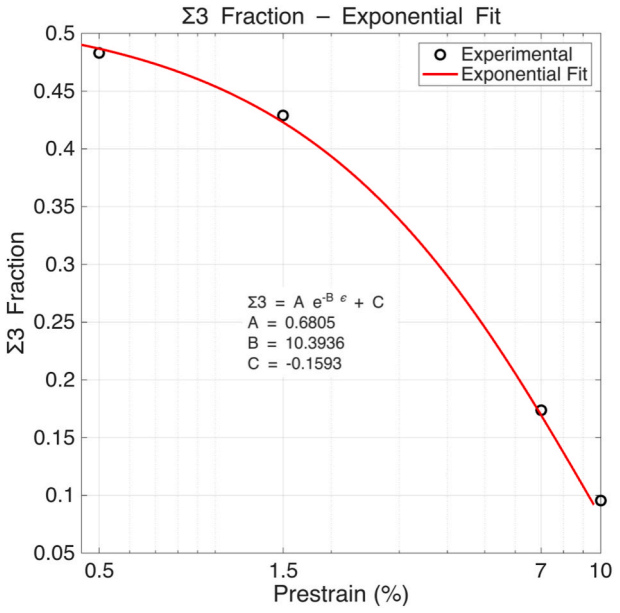

Fig. 9. Σ3 boundary fraction as a function of prestrain. Black symbols denote the experimentally measured Σ3 fractions at prestrain of 0.5 %, 1.5 %, 7 %, and 10 %. The red curve represents the exponential fit. The fitting was performed using true strain values. The fitted equation and constants are included in the figure.

The close correspondence between the model predictions and the experimentally measured true stress-strain curve suggests that the reduction and fragmentation of Σ3 boundaries play a crucial role in

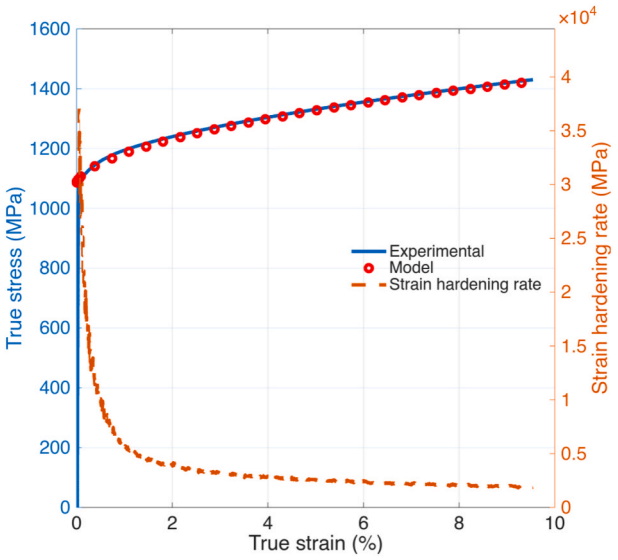

Fig. 10. True stress–true strain response for the 10 % prestrained condition, used for calibration of the constitutive model parameters and Strain hardening rate as a function of true strain for the 10 % prestrain condition.

determining the mechanical response of aged IN718. This confirms that the proposed model effectively represents the underlying deformation and hardening mechanisms during tensile deformation. Since back stress originates primarily from long-range internal stresses caused by dislocation structures and interactions with microstructural features, its evolution is intrinsically linked to the factors that influence flow stress. Back stress arises from long-range internal stresses associated with dislocation structures and their interactions with microstructural barriers, and its evolution is inherently influenced by the same mechanisms that control flow stress. Therefore, although the present dislocation-based framework directly predicts flow stress, the trends observed in back stress evolution are attributed to analogous underlying dislocation–boundary interactions.

In addition to a change in Σ3 boundary fraction, dislocation substructure is another factor influencing the variation in the rate of back stress. At low prestrain, the dislocation density increases gradually, as shown in Fig. 6, and well-organised dislocation substructures, such as GNBs, are not observed. As prestrain increases, a significant rise in GND density is observed, accompanied by the formation of GNBs, as shown in Fig. 4 (a). As the GNBs regulate dislocation slip, just as the initial grain boundaries do [34], dislocations accumulate more. This transition likely contributes to the increased back stress at higher prestrain.

In addition to grain boundary character and the variation in dislocation density, both the shearing of γ" precipitates [42] (dislocation-precipitate interaction) and their morphology may influence back stress evolution in IN718. The disc-shaped morphology of γ" precipitates, along with their specific orientation relationship with the γ matrix, may reduce elastic-plastic anisotropy and deformation incompatibility at grain boundaries, as reported in previous study [12]. In the current study, at low prestrain levels, the shearing of γ" precipitates may be limited due to relatively lower stress, and this short-range interaction may contribute to back stress. However, as the prestrain increases, γ" precipitates experience substantial shearing. This change in precipitate response may bring an additional mechanism behind the shift in back stress rate observed at low and high prestrain. Overall, in IN718, back stress evolution is governed by the interplay between grain boundary character, dislocation substructures, and dislocation-γ" precipitate interactions.

While the study provides insights into the correlation between GND density, Σ3 boundaries, and back stress, it is limited to uniaxial tensile prestrain. Authors acknowledge that back stress evolution is known to

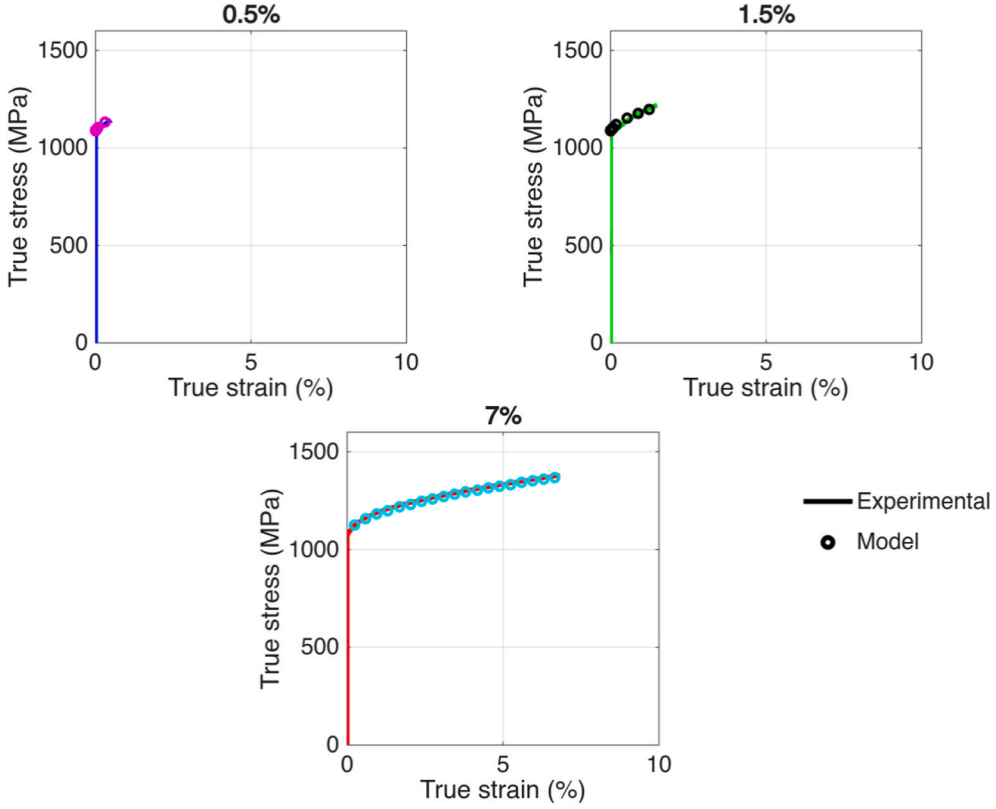

Fig. 11. Comparison between experimentally measured and model-predicted true stress–true strain curves for 0.5 %, 1.5 %, and 7 % prestrain conditions. The model predictions are generated using the parameter set calibrated from the 10 % prestrain case.

be path-dependent, and different loading paths (compression, shear, or multi-axial) may produce distinct mechanisms and magnitudes of back stress.

Earlier studies have generally attributed back stress to mechanisms such as precipitate shearing versus looping, carbide-controlled slip localisation, or deformation incompatibility associated with γ''/γ' strengthening phases [9,10,12]. For example, Kreins et al. demonstrated that γ'' precipitation affects slip planarity and GND distributions in IN718, and that specific nanoscale γ'' conditions can even mitigate the Bauschinger effect by promoting more homogeneous grain-scale deformation; however, their study did not investigate the role of Σ3 boundaries, which are prevalent in Ni-based superalloys. Prestraining studies on IN718 [35] have also reported reductions in Σ3 boundaries, accompanied by increases in dislocation density; however, these microstructural changes were not linked to back stress behaviour. In contrast, the present study demonstrates, for the first time, that the reduction of Σ3 boundaries with increasing prestrain is directly associated with the rise in back stress in aged IN718. By establishing a mechanistic pathway that connects the evolution of Σ3 boundaries, GND density, and macroscopic back stress, this work identifies a Σ3-controlled mode of back stress evolution that operates in conjunction with previously proposed precipitate- and phase-controlled mechanisms. This comparison highlights the uniqueness of the current findings and underscores the critical role of Σ3 boundary distribution—a factor overlooked in earlier back stress studies on IN718.

The present study quantifies both macroscopic and microscopic back stress. The microscopic back stress is derived using three distinct approaches: (1) the KAM-based method, (2) the Nye tensor method, and (3) Ashby's model. A comparison between the microscopic and macroscopic back stress demonstrates that the trends obtained from both methods closely align, as shown in Fig. 7, thereby confirming the reliability of these approaches. The microscopic back stress calculated using the KAM-based and Nye tensor methods for prestrain levels of 0.5 % and 1.5 % shows more favourable trends than those predicted by Ashby's model. Furthermore, the KAM-based and Nye tensor methods accurately predict the back stress rates at both low and high prestrain levels, indicating that these approaches are better suited for determining microscopic back stress at small prestrain levels. While all methods indicate nearly similar trends, they do possess certain limitations. Ashby's model provides a simplified empirical estimate of GND density but lacks microstructural correlation. The Nye tensor and KAM-based methods, relying on 2D EBSD data, have limitations: the Nye tensor excludes out-of-plane components. In contrast, the KAM-based approach may smooth local variations due to averaging. Both are also sensitive to EBSD resolution and noise. Despite these constraints, they provide reasonable approximations for quantifying microscopic back stress and are explored in this study to enhance the understanding of back stress evolution.

6. Conclusion

This work provides new insights into back stress evolution in aged Inconel 718 under varying prestrain through tension (prestrain)-compression tests. The following conclusions can be derived :

- A direct comparison between macroscopic back stress, obtained from stress-strain data from a tensile test followed by compression, and microscopic back stress, quantified using GND density through a Taylor-type equation, has been performed experimentally for the first time. The consistency and agreement between these two approaches validate the methodology. Among microscopic back stress estimation methods, the KAM-based and Nye tensor approach effectively captured trends, especially at lower prestrain, compared to Ashby's model.
- The difference in the rate of back stress evolution is observed for low prestrain and high prestrain. For prestrain of 0.5 % and 1.5 %, back stress was primarily attributed to the little contribution from all grain boundaries, dislocation substructures and dislocation-γ'' precipitates interaction, which can be confirmed by lower GND density and lower mean KAM value near grain boundaries.
- In contrast, at higher prestrain, 7 % and 10 %, the back stress increased significantly, driven by contributions from grain boundaries and dislocation substructures as the γ'' precipitates were likely sheared. This was supported by higher GND density, increased KAM value near grain boundaries and reduced Σ3 boundaries with increasing prestrain.
- The dislocation-based model has been modified to incorporate the effect of the reduction in Σ3 boundaries. The strong consistency observed between the experimentally measured true stress-strain curve and the model predictions confirms that the reduction of Σ3 boundaries is a key mechanism contributing to the increase in flow stress. This microstructural change also plays a significant role in the development of back stress during deformation.

Declaration of competing interest

The authors declare that they have no known competing financial interests or personal relationships that could have appeared to influence the work reported in this paper.

Acknowledgements

The authors acknowledge the International Cooperative Graduate Program (ICGP) of the NIMS, Japan. This study is based on work partially supported by a Grant-in-Aid for Scientific Research (Grant No. 23H01732) from the Japan Society for the Promotion of Science (JSPS).

References

[1] Reed RC. The superalloys: fundamentals and applications. Cambridge University Press; 2006.
[2] Bauschinger J. Mittheilung XV: on the changes of the elastic limit and the strength of iron by straining in tension and in compression. Mittheilungen aus dem Mechanisch-Technischen Laboratorium der Königlichen Technischen Hochschule in München 1886;13:1–115.
[3] Mahato JK, De PS, Sarkar A, Kundu A, Chakraborti PC. Effect of deformation mode and grain size on Bauschinger behaviour of annealed copper. Int J Fatig 2016;83:42–52.
[4] Mahato JK, De PS, Sarkar A, Kundu A, Chakraborti PC. Effect of prestrain and stress rate on bauschinger effect of monotonically and cyclically deformed OFHC copper. Procedia Eng 2014;74:368–75.
[5] Feaugas X, Haddou H. Grain-size effects on tensile behaviour of nickel and AISI 316L stainless steel. Metall Mater Trans 2003;34:2329–40.
[6] Gao S, Yoshino K, Terada D, Kaneko Y, Tsuji N. Significant Bauschinger effect and back stress strengthening in an ultrafine-grained pure aluminium fabricated by severe plastic deformation process. Scr Mater 2022;211.
[7] Queyreau S, Devincre B. Bauschinger effect in precipitation-strengthened materials: a dislocation dynamics investigation. Philos Mag Lett 2009;89:419–30.
[8] Kreins M, Wilkes J, Krupp S Wesselmecking U. Effect of phase-selective nanoscale precipitates on the bauschinger effect in austenitic–ferritic Duplex stainless steels. Metall Mater Trans 2022;53(11):3906–17.
[9] Thakur A, Nemat-Nasser KS Vecchio S. Bauschinger effect in Haynes 230 alloy: influence of strain rate and temperature. Metall Mater Trans 1996;27(7):1739–48.
[10] A del Valle J, Romero R, Picasso AC. Bauschinger effect in age-hardened Inconel X-750 alloy. Materials Science and Engineering: A 2001;311(1–2):100–7.
[11] He W, Wan M, Meng B. Size effect on nonlinear unloading behaviour and Bauschinger effect of Ni-based superalloy ultrathin sheet. Int J Mech Sci 2022;231.
[12] Kreins M, Büßenschütt K, Wesselmecking S, Krupp U. On the impact of nanoscale γ'' precipitates on the Bauschinger effect in single- and polycrystal Ni-base superalloy 718. Materials Science and Engineering: A 2022;856.
[13] Han K, Tyne CJV, Levy BS. Effect of strain and strain rate on the Bauschinger effect response of three different steels. Metall Mater Trans 2005;36(9):2379–84.
[14] Sohn SS, Han SY, Shin SY, Bae J, Lee S. Effects of microstructure and pre-strain on Bauschinger effect in API X70 and X80 line pipe steels. Met Mater Int 2013;19:3.
[15] Zhu Y, Wu X. Perspective on hetero-deformation induced (HDI) hardening and back stress. Mater Res Lett 2019;7:393–8.
[16] Hielscher R, Schaeben H. A novel pole figure inversion method: specification of the MTEX algorithm. J Appl Crystallogr 2008;41(6):1024–37.
[17] Bachmann F, Hielscher R, Schaeben H. Grain detection from 2d and 3d EBSD data-Specification of the MTEX algorithm. Ultramicroscopy 2011;111:1720–33.

[18] Fribourg G, Bréchet Y, Deschamps A, Simar A. Microstructure-based modelling of isotropic and kinematic strain hardening in a precipitation-hardened aluminium alloy. Acta Mater 2011;59:3621. 2625.
[19] Moan GD, Embury JD. A study of the Bauschinger effect in AlCu alloys. Acta Metall 1979;27:903–14.
[20] Thom CA, Hansen LN, Breithaupt T, Goldsby DL, Kumamoto KM. Back stresses in geologic materials quantified by nanoindentation load-drop experiments. Philos Mag 2022;102:19–2022.
[21] Thom CA, Hansen LN, Goldsby DL, Brodsky EE. A microphysical model of rock friction and the brittle-ductile transition controlled by dislocation glide and back stress evolution. J Geophys Res Solid Earth 2023;128:12.
[22] Jiang J, Britton TB, Wilkinson AJ. Measurement of geometrically necessary dislocation density with high-resolution electron backscatter diffraction: effects of detector binning and step size. Ultramicroscopy 2013;125:1–9.
[23] Pantleon W. Resolving the geometrically necessary dislocation content by conventional electron backscattering diffraction. Scr Mater 2008;58:994–7.
[24] Jiang J, Britton TB, Wilkinson AJ. Evolution of dislocation density distributions in copper during tensile deformation. Acta Mater 2013;61:7227–39.
[25] Calcagnotto M, Ponge D, Demir E, Raabe D. Orientation gradients and geometrically necessary dislocations in ultrafine-grained dual-phase steels studied by 2D and 3D EBSD. Materials Science and Engineering: A 2010;527:2738–46.
[26] Härtel M, Illgen C, Bruder E, Frint P, Wagner MF-X. Microstructural evolution during uniaxial tension-compression in-plane deformation of an IF steel. Materials Science and Engineering: A 2019;744:652–60.
[27] Zhu C, Harrington T, Gray GT, Vecchio KS. Dislocation-type evolution in quasi-statically compressed polycrystalline nickel. Acta Mater 2018;155:104–16.
[28] Ashby MF, et al. The deformation of plastically non-homogeneous materials. The philosophical magazine. J Theor Exp Appl Phy 1970;21:399–424.
[29] Foley DL, Latypov MI, Zhao X, Hestroffer J, Beyerlein IJ, Lamberson LE, Taheri ML. Geometrically necessary dislocation density evolution as a function of microstructure and strain rate. Materials Science and Engineering: A 2022:831.
[30] Gallet J, Perez M, Guillou R, Ernould C, Bourlot CL, Langlois C, Beausir B, Bouzy E, Chaise T, Cazottes S. Experimental measurement of dislocation density in metallic materials: a quantitative comparison between measurement techniques (XRD, R-ECCI, HR-EBSD, TEM). Mater Char 2023;199:112842.
[31] Agaram S, Srinivasan SM, Bhuvaraghan B, Kanjarla AK. Dislocation density-based crystal plasticity model incorporating the effect of precipitates in IN718 under monotonic and cyclic deformation. Int J Plast 2021;141:102990.
[32] Agaram S, Srinivasan SM, Kanjarla AK. Crystal plasticity modelling of stability of residual stresses induced by shot peening. Int J Mech Sci 2022;230:107526.
[33] Han K, Tyne CJV, Levy BS. Effect of strain and strain rate on the Bauschinger effect response of three different steels. Metallurgical and Materials Transaction A 2005; 36:2379–84.
[34] Kuhlmann-Wilsdorf D, Hansen N. Geometrically necessary, incidental and subgrain boundaries. Scripta Metall Mater 1991;25(7):1557–62.
[35] Zhu J, Yuan W. Effect of pre-stretching on residual stresses and microstructures of inconel 718 superalloy. Metals 2021;11:614.
[36] Lin Y, Han L, Wang G. Relationship between Σ3 boundaries, dislocation slip, and plasticity in pure nickel. Materials 2023;16:2853.
[37] Kapoor K, Yoo YSJ, Book TA, Kacher JP, Sangid MD. Incorporating grain-level residual stresses and validating a crystal plasticity model of a two-phase Ti-6Al-4V alloy produced via additive manufacturing. J Mech Phys Solid 2018;121:447–62.
[38] Bandyopadhyay R, Gustafson SE, Kapoor K, Naragani D, Pagan DC, Sangid MD. Comparative assessment of backstress models using high-energy X-ray diffraction microscopy experiments and crystal plasticity finite element simulations. Int J Plast 2021;136:102887.
[39] Bouaziz O, Guelton N. Modelling of TWIP effect on work-hardening. Materials Science and Engineering: A 2001;319–321:246–9.
[40] Lavrentev FF. The type of dislocation interaction as the factor determining work hardening. Mater Sci Eng 1980;46:191–208.
[41] Malmelöv A, Fisk M, Lundbäck A, Lindgren L-E. Mechanism-based flow stress model for Alloy 625 and Alloy 718. Materials 2020;13:5620.
[42] Sundararaman M, Mukhopadhyay P, Banerjee S. Deformation behaviour of γ″ strengthened Inconel 718. Acta Metall 1988;36:847–64.